

Article

Water-Quality Monitoring with a UAV-Mounted Multispectral Camera in Coastal Waters

Alejandro Román ^{1,*}, Antonio Tovar-Sánchez ¹, Adam Gauci ², Alan Deidun ², Isabel Caballero ¹, Emanuele Colica ², Sebastiano D'Amico ² and Gabriel Navarro ¹

¹ Department of Ecology and Coastal Management, Institute of Marine Sciences of Andalusia (ICMAN), Spanish National Research Council (CSIC), 11510 Cádiz, Spain

² Department of Geosciences, University of Malta (UM), MSD 2080 Msida, Malta

* Correspondence: a.roman@csic.es

Abstract: Remote-sensing ocean colour studies have already been used to determine coastal water quality, coastal biodiversity, and nutrient availability. In recent years, Unmanned Aerial Vehicles (UAVs) equipped with multispectral sensors, originally designed for agriculture applications, have also enabled water-quality studies of coastal waters. However, since the sea surface is constantly changing, commonly used photogrammetric methods fail when applied to UAV images captured over water areas. In this work, we evaluate the applicability of a five-band multispectral sensor mounted on a UAV to derive scientifically valuable water parameters such as chlorophyll-a (*Chl-a*) concentration and total suspended solids (TSS), including a new Python workflow for the manual generation of an orthomosaic in aquatic areas exclusively based on the sensor's metadata. We show water-quality details in two different sites along the Maltese coastline on the centimetre-scale, improving the existing approximations that are available for the region through Sentinel-3 OLCI imagery at a much lower spatial resolution of 300 m. The *Chl-a* and TSS values derived for the studied regions were within the expected ranges and varied between 0 to 3 mg/m³ and 10 to 20 mg/m³, respectively. Spectral comparisons were also carried out along with some statistics calculations such as RMSE, MAE, or bias in order to validate the obtained results.



Citation: Román, A.; Tovar-Sánchez, A.; Gauci, A.; Deidun, A.; Caballero, I.; Colica, E.; D'Amico, S.; Navarro, G. Water-Quality Monitoring with a UAV-Mounted Multispectral Camera in Coastal Waters. *Remote Sens.* **2023**, *15*, 237. <https://doi.org/10.3390/rs15010237>

Academic Editors: Riccardo Roncella and Ricardo Torres

Received: 28 November 2022

Revised: 23 December 2022

Accepted: 27 December 2022

Published: 31 December 2022



Copyright: © 2022 by the authors. Licensee MDPI, Basel, Switzerland. This article is an open access article distributed under the terms and conditions of the Creative Commons Attribution (CC BY) license (<https://creativecommons.org/licenses/by/4.0/>).

1. Introduction

Coastal waters constitute a complex, variable, and highly dynamic ecosystem. Bays and ports not only provide shelter for a rich biodiversity of aquatic fauna and flora, but also offer a range of ecosystem services of great economic value to human societies [1,2]. However, the recent surge in coastal activities such as aquaculture, tourism, and in blue economy sectors, has led to the disturbance of the ecological structure of the coastal marine environment as well as to a progressive nutrient enrichment of coastal waters. In turn, this is promoting phenomena such as eutrophication, hypoxia, or the death of aquatic animal and plant species [2–4]. This is due to the fact that the increase in levels of dissolved phosphorus and nitrogen in coastal waters can lead to excessive growth of algae, phytoplankton, and vegetation close to the water surface [5]. Concurrently, globally rising temperatures are reducing phytoplankton productivity. The increase in atmospheric concentrations of carbon dioxide (CO₂) are also diminishing the efficiency of the ocean's biological carbon pump, adding further stress to already overfished fishery stocks [6,7].

The chlorophyll-a (*Chl-a*) concentration is commonly used as an indicator to assess the biogeochemical status of surface waters (e.g., within Descriptor 5 of the Marine Strategy Framework Directive—MFSD—as well as a Biological Quality Element (BQE) in the Water Framework Directive—WFD), as well as to monitor changes in the primary productivity

of phytoplankton [1,5]. This concentration also gauges the extent of eutrophication in coastal surface waters as it is indicative of nutrient availability [2,4,8]. The amount of the total concentration of suspended solids (TSS) is also used to monitor the quality of the water given its direct impact on light scattering and penetration in the water column and its indirect impact on benthic biota once the suspended solids settle on the seabed. The TSS concentration is also directly related to the transfer of contaminants such as heavy metals and organics [4,9]. Changes in the *Chl-a* and TSS concentrations affect ocean colour and are indicative of the surface water's contamination status. The monitoring of these two parameters is thus essential in assessing the biogeochemical conditions of coastal waters for the conservation of water resources, especially in those regions most affected by human activities [1,4].

Traditional methods for water-quality monitoring required the collection of in situ water samples and a subsequent laboratory analysis for the extraction of the optical properties of water [1,3,4,10]. However, despite their high degree of analytical accuracy, these techniques are time-consuming, labor-intensive, and expensive [4,10,11]. Moreover, they are inadequate to monitor variations in water-quality parameters over a large area [5]. With technological advances in remote sensing, ocean colour studies from satellite imagery have made global observations of coastal and oceanic regions possible [12]. These techniques are based on algorithms that utilize remote sensing reflectance (*Rrs*) values to derive water-quality parameters such as turbidity, photosynthetic pigment concentration, and coloured, dissolved organic matter (CDOM) [3,13–15]. Several studies (such as those by [4,11,16–24]) have proposed the use of such a tool to complement conventional techniques as it could help in operational water-quality monitoring due to its high efficiency, convenient acquisition time, low cost, and wide coverage. However, coastal regions are spectrally complex and monitoring through satellite remote sensing is challenging due to two fundamental factors [1]. Primarily, the occurrence of cloud covers can leave areas without information for long periods of time, especially if this coincides with the satellite passage temporal window [3,14]. Secondly, the instruments on board most of the satellites, such as the Moderate Resolution Imaging Spectroradiometer (MODIS), the Medium Resolution Imaging Spectrometer (MERIS), and the Ocean and Land Colour Instrument (OLCI), are designed to measure water quality in open waters with a coarse spatial resolution [4,11,14,25]. This is inadequate for coastal areas or small islands such as Malta. Although in the last few years several advancements in ocean colour remote-sensing protocols have been registered, issues related to the spectral and temporal gaps that do not allow for sub-mesoscale information to be acquired still persist [26].

Unmanned Aerial Vehicles (UAVs) have gained global popularity as a remote-sensing tool as they address the optical challenges of water-quality studies in coastal regions. These UAV-based methods provide ultra-high resolution (centimetre-scale range, for instance). The temporal frequency of data acquisition can be controlled and is only limited by sea-surface weather conditions. Clouds do not affect data collection. Moreover, UAVs are much cheaper to procure and operate than other remote-sensing tools [3,13,26,27]. Various lightweight sensors can be mounted to measure optical RGB, thermal, multispectral, and LiDAR bands to estimate in-turn values for a range of water-quality parameters similar to those obtained by satellite, such as sea surface temperature (SST), TSS, *Chl-a*, and total nitrogen or total phosphorus [11].

Although a number of structure from motion (SfM) photogrammetry techniques are available, these use a combination of numerical methods to generate georeferenced reflectance maps by identifying and stitching common points in different photos. Since the surface of the sea is constantly changing, such methods fail when applied to images captured when UAVs fly over water [26]. That is why most water-quality studies that use these tools are limited to the coastline (e.g., [11,25,28]), or to small water bodies such as lakes and reservoirs (e.g., [14,29,30]). Instead of SfM photogrammetry, ref. [15] proposed to obtain *Rrs* measurements directly from the UAV captures. Ref. [27] presented a single algorithm for retrieving water-quality parameters directly from UAV multispectral captures. In their

study, they successfully tested four approaches to remove sun glint and surface-reflected light to derive *Chl-a* and TSS concentrations. UAV multispectral imagery was used in [3] to retrieve remote-sensing reflectance (*Rrs*) for a *Chl-a* estimation in an extremely turbid coastal study case in Saemangeum (South Korea). The authors also managed to observe small-scale ocean dynamics that could help to identify red tide patches or coastal blooms.

In this study, we evaluate the applicability of the method presented by [27] for retrieving *Rrs* data from the individual captures obtained with a five-band multispectral sensor mounted on a UAV. In addition, the methodology put forward in [27] is updated with respect to when to process and stitch together individual captures. A novel Python workflow is implemented to manually generate an orthomosaic over the water area. Simultaneously, structure from motion (SfM) photogrammetry is applied to UAV data, being used as a reference to compare and validate the results obtained with the processed individual captures. The results obtained are compared on a band-by-band and a pixel-by-pixel basis, and statistics such as RMSE, MAE, and bias are calculated. Finally, the water-quality parameters are obtained through the application of different algorithms (OC-2 [31] and OC-3 [32] for *Chl-a* and [33] for TSS) to UAV and S2 *Rrs* data. This study represents the first open-source approach for the generation of orthomosaics using UAV data in aquatic regions, setting a basis for subsequent studies of water quality in coastal and oceanic regions.

2. Materials and Methods

2.1. Study Area

With a population density of around 1500 people per m^2 , the Maltese archipelago (Figure 1), constitutes one of the most densely populated countries in the world. In recent years, the levels of tourism activities have increased, and approximately two million tourists visit Malta, Gozo, and Comino (the three main islands) per year [34,35]. For this reason, the Maltese coastal waters are subject to a wide range of anthropogenic activities that exert pressure which may impact the quality of the environment. Several studies (such as [36,37]) indicated that the dense and healthy *Posidonia oceanica* (L.) Delile meadows populate the seabed along the northeast coast of the Maltese islands, extending in some cases to depths of up to 43 m [38]. This seagrass species is one of the most productive and abundant in the world, and it constitutes one of the most important coastal ecosystems as it acts as a feeding and nursery refuge for numerous animal species due to its function as a carbon sink [37].

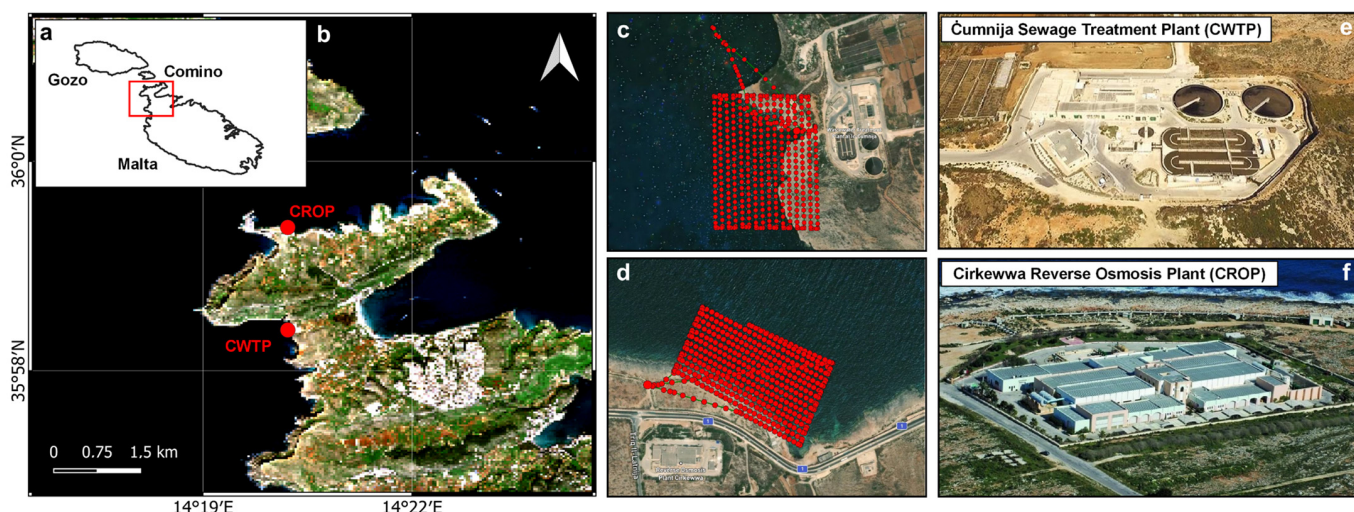


Figure 1. (a) Map showing the three islands that constitute the Maltese Islands archipelago: Malta, Gozo and Comino. (b) Zoom made on the Sentinel-2 image that shows the northeast coast of the island of Malta, where they are located: (c) flight plan at the Ćumnija Sewage Treatment Plant (CSTP); (d) flight plan at the Cirkewwa Reverse Osmosis Plant (CROP); and (e,f) real images of CSTP and CROP, respectively.

Other significant sources of pollution in the Maltese coastal waters include sewage treatment plants that sometimes malfunction and release untreated outflow into the sea. RO plants that supply fresh water to a significant percentage of the island also discharge brine solution into the sea and may affect the health of *P. oceanica* [39]. In this study, UAV surveys were carried out in the northeast part of the island of Malta at the Ċumnija Sewage Treatment Plant (CSTP) and close to the Cirkewwa Reverse Osmosis Plant (CROP) that are shown in Figure 1. These sites were chosen as polluted discharges could give rise to biogeochemical changes that, in turn, may lead to variations in the water-quality indicators. CSTP was inaugurated in January 2009 and has the capacity to treat 6700 m³ of wastewater per day. CROP was inaugurated in 1982 and has the capacity to treat 18,600 m³ of water per day [34].

2.2. Sentinel-2 Imagery

In this study, data from the twin, polar-orbiting Sentinel-2A and Sentinel-2B (S2) satellites from the European Commission and the European Space Agency (ESA) were used to obtain detailed information on the characteristics of the Maltese coastal waters. The Level 1 top-of-atmospheric (TOA) reflectance products derived from the S2 MultiSpectral Instruments (MSI), whose characteristics are detailed in ESA's Handbook [40,41], were corrected using the ACOLITE software (version 20220222.0) to generate the bottom-of-atmosphere (BOA) Level 2A products. The dark spectrum fitting (DSF) atmospheric correction algorithm was applied. A sun-glint correction over the surface reflectance by means of the additional, image-based sun-glint correction was also performed [42,43]. The data resampled at a 10 m spatial resolution were obtained from the Copernicus Open Access Hub (<https://scihub.copernicus.eu/>, accessed on 2 May 2022) using the tile T33SVV.

2.3. UAV Operations and Data Collection

A DJI Matrice 600 Pro (M600) UAV equipped with a multispectral MicaSense RedEdge-MX sensor was used to acquire aerial images over the Maltese coastline (Figure 1). The M600 Pro is a 10 kg hexacopter with a DJI 6010 propulsion system powered by six LiPo 6S batteries (4500 mAh each) whose maximum takeoff weight (MTOW) is 15.5 kg. The multispectral camera that was mounted on the M600 Pro is capable of capturing simultaneous images of the blue (475 nm), green (560 nm), red (668 nm), red edge (717 nm), and NIR (842 nm) bands. This camera allows for the obtaining of 8 cm/pixel captures at 120 m altitude and includes a downwelling light sensor (DLS) that has a built-in GPS and inertial measurement unit (IMU). This made more accurate and reliable measurements of the downwelling irradiance and the solar angle possible during in-flight image captures. A calibration panel (RP04-1934108-OB) was also used for radiometric calibration.

The UAV surveys were carried out on the morning of the 4 May 2022, with clear skies and favorable meteorological conditions. The altitude was set to 50 m to achieve a ground sampling distance (GSD) of 3.47 cm/pixel. The flight was planned using the Pix4D Capture (Pix4D SA, Lausanne, Switzerland) software and considered a front overlap of 85% and a side overlap of 75%. Prior to the flights, captures at a 40° angle were taken to compute the sky radiance (L_{sky}) measurements. L_{sky} was computed by following the method proposed by [27]. Information about solar elevation, image size, positioning, and orientation of each image capture was also recorded in the metadata of the multispectral camera.

2.4. Data Processing

Figure 2 represents the methodological workflow followed in this study. In order to retrieve Rrs data from the individual radiometric UAV captures, the methodology proposed by [27] was followed, testing the dark pixel assumption (DPA) and “deglinting” (DEG) processing techniques. The results obtained via these methods were statistically validated, with UAV Rrs data retrieved from SfM photogrammetry considered as the reference data due to the logistical difficulties of obtaining in situ water samples during the UAV surveys.

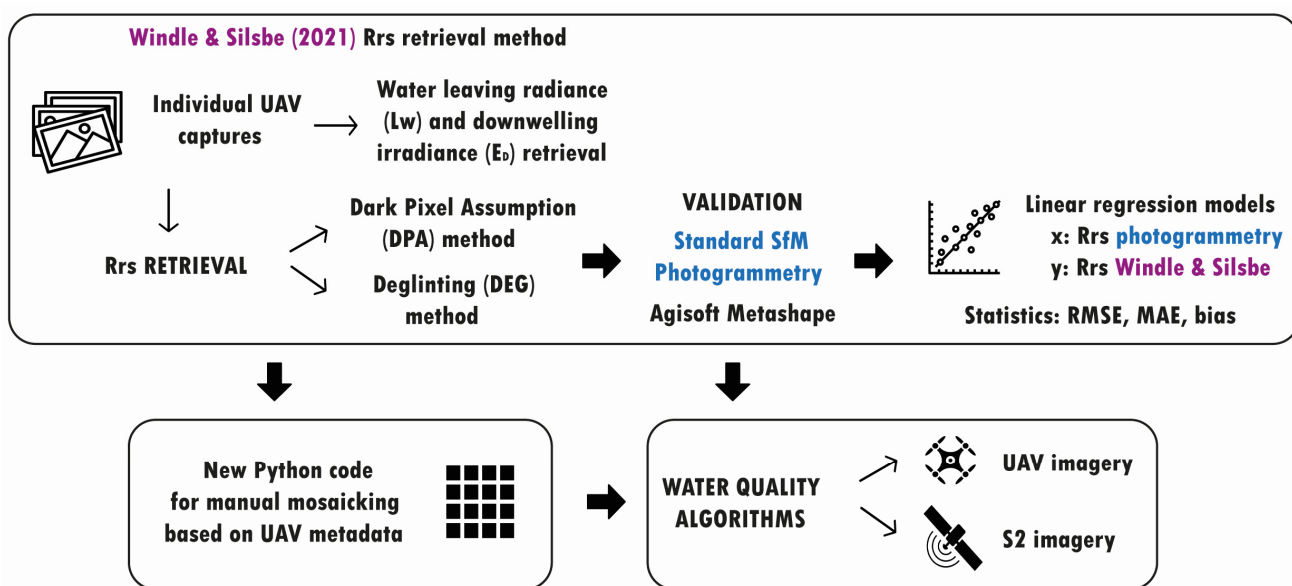


Figure 2. Methodological workflow followed in the present study [27].

Subsequently, the *Rrs* data retrieved at each individual UAV capture were processed by a novel Python workflow (see Supplementary Material) to generate an orthomosaic over the water area. The code is based not only on the yaw, pitch, and roll of the UAV, but also on the latitude and longitude information provided by the MicaSense metadata during the surveys.

Finally, the spectral response of the Maltese coastal waters was analysed through the representation of spectral signatures using UAV and satellite imagery. In addition, the water-quality parameters were then obtained through the application of the aforementioned *Chl-a* and TSS algorithms on UAV and S2 *Rrs* data.

2.4.1. UAV SfM Photogrammetry

Agisoft Metashape v.1.8.3 (Agisoft LLC, St. Petersburg, Russia) was used to process the multispectral images for the generation of orthomosaics from the UAV captures. This software created an orthomosaic of *Rrs* values for each multispectral band. After importing the selected images, a 3D, sparse point cloud was reconstructed by performing “capture alignment”. This was carried out with the highest accuracy setting. The “ground control” option was selected, and the tie points limits were set to 40,000 for the complete dataset. A 3D, densepoint cloud was then generated using an “aggressive” depth filter and an “ultrahigh” quality setting to minimise outliers in the reconstruction. An interpolated digital elevation model (DEM) was then generated from the created “dense cloud.” Finally, an orthomosaic was rendered for each of the multispectral bands using the DEM as a reference surface. In this case, the “mosaic” was created using the blending mode. Sun-glint reflection over the water was masked by creating manual polygons and replacing overexposed areas with the computed average value of the surrounding pixels. The resulting orthomosaics were projected to WGS84/UTM zone 33N (EPSG: 32633), and a final spatial resolution of 3.47 cm/pixel was achieved.

2.4.2. Remote-Sensing Reflectance Retrieval from UAV Individual Captures

As shown in Equation (1), *Rrs* is ultimately derived from the water-leaving radiance (*L_w*) and the downwelling irradiance just above the surface (*E_D*) [3,27,44].

$$R_{rs}(sr^{-1}) = \frac{L_w (W m^{-2} nm^{-1} sr^{-1})}{E_D (W m^{-2} nm^{-1})} \quad (1)$$

For UAV measurements, the water-leaving reflectance (L_w , Equation (2)) results from equations that consider at-sensor total radiance (L_T) and the surface-reflected radiance (L_{SR}), which can be defined as the incident radiance reflected off the sea surface into the detector's field of view [27].

$$L_T \left(\text{W m}^{-2} \text{nm}^{-1} \text{sr}^{-1} \right) = L_W \left(\text{W m}^{-2} \text{nm}^{-1} \text{sr}^{-1} \right) + L_{SR} \left(\text{W m}^{-2} \text{nm}^{-1} \text{sr}^{-1} \right) \quad (2)$$

The raw data obtained with the RedEdge multispectral camera are given as digital numbers (DN), and their values are affected by atmospheric factors such as absorption or scattering. To convert to radiance, the radiometric calibration process provided by MicaSense [45] was used. This follows the method proposed by [27] which is formalised using Equation (3) to convert the raw pixels values into L_T values ($\text{W m}^{-2} \text{nm}^{-1} \text{sr}^{-1}$).

$$L_T \left(\text{W m}^{-2} \text{nm}^{-1} \text{sr}^{-1} \right) = V(x, y) * \frac{a_1}{g} * \frac{P - P_{BL}}{t_e + a_2 y - a_3 t_e y} \quad (3)$$

Here, $V(x, y)$ is the lens vignette effect for each pixel location (x, y) ; a_1 , a_2 , and a_3 are the radiometric calibration coefficients; g is the sensor setting; P is the normalized raw DN; P_{BL} is the normalized dark pixel value; and t_e are exposure settings.

The calculated L_{sky} , E_D , and L_T were used to estimate L_{SR} using two different methods: (i) the “dark pixel assumption ($NIR = 0$)” method (DPA), and (ii) the “deglinting” method (DEG) proposed by [46,47]. Generally, for clear waters, the DPA method allows for the ignoring of the L_w of the NIR that equals to 0, implying a reduction in the influence of the scattering, the white cap, and sun glint by subtracting reflectance at the NIR wavelength [48]. Thus, Rrs can be calculated for all bands from Equation (4), where R_{TOT} represents the UAV total reflectance:

$$Rrs \left(\text{sr}^{-1} \right) = R_{TOT} - \frac{L_{sky} * \left(\frac{L_T(NIR)}{L_{sky}(NIR)} \right)}{E_D} \quad (4)$$

Following [47], the DEG method (Equation (5)) made a linear regression between all R_{TOT} (NIR) and R_{TOT} (visible) values, determining the slope (b_i). Each pixel was corrected by subtracting the product of b_i and the NIR brightness of the pixel. A minimum NIR value was also determined from the lowest 10% of R_{TOT} (NIR) across all captures [27]:

$$Rrs \left(\text{sr}^{-1} \right) = R_{TOT} - b_i(R_{TOT}(NIR) - \min(R_{TOT}(NIR))) \quad (5)$$

The MicaSense workflow [45], which uses the metadata (such as the yaw, the pitch, the roll and the geographic position of the UAV) to georeference the individual captures by the multispectral sensor, was followed. This was achieved with the CameraTransform Python package [48], which works directly with the sensor metadata without considering the changes in the capture orientation depending on the UAV flight direction. For this reason, by default, the code outputs appear flipped in certain image capture positions, so that the “heading_deg” parameter should be set as 0° (when the UAV is heading East), 90° (when the UAV is heading North), 180° (when the UAV is heading West), or 270° (when the UAV is heading South). The developed Python code generated two data matrices, one of them including values of the variable (in this case Rrs , $Chl-a$, or TSS), and another transformation matrix that detected the metadata acting as a basis on which the merging process is carried out. The code then walked through each of the individual captures, assigning them to their corresponding position according to their geographic positions and thereby filling the final data matrix. Once it was filled, the average value of each of the individual captures that overlap each other was calculated without considering NaN values. Both the georeferencing and merging methods are provided as Supplementary Materials.

2.4.3. Accuracy Assessment

To determine which reflectance-retrieval method performed better, a band-by-band as well as a pixel-by-pixel correlation between each of the individual RedEdge-MX captures and the orthomosaic obtained by SfM photogrammetry was carried out. In particular, a linear regression model was applied to the 100 randomly extracted pixels for each spectral band. To validate the consistency between data, the coefficient of determination (R^2), the root mean square error (RMSE) as defined in Equation (6), the mean absolute error (MAE) given by Equation (7), and the bias as formalised in Equation (8), were computed between pairs.

$$RMSE = \sqrt{\frac{\sum_{i=1}^n (O_i - M_i)^2}{n}} \quad (6)$$

$$MAE = \frac{\sum_{i=1}^n |O_i - M_i|}{n} \quad (7)$$

$$bias = \frac{\sum_{i=1}^n (O_i - M_i)}{n} \quad (8)$$

here i represents each classification cover class, M_i represents the UAV data considered as reference values, O_i represents the satellite data, and n is the sample size ($n = 20$) [49].

2.4.4. Spectral Comparison

Prior to the application of water-quality algorithms, a shape spectrum analysis at several pure water pixels between the Rrs obtained from UAV and S2 imagery was performed. The Rrs was standardized to prioritize the influence of the shape spectrum by reducing variability in Rrs values associated with shadowing, sun glint, and seafloor shallowing. Consequently, the comparison between the spectral signatures of different sensors was facilitated by using the standardization Min-Max [50] method on Rrs values, following the Equation (9):

$$x_{ij}^* = \frac{x_{ij} - \min(x_{ij})}{\max(x_{ij}) - \min(x_{ij})} \quad (9)$$

where $\min(x_{ij})$ is the minimum reflectance value of the reflectance spectrum and $\max(x_{ij})$ the maximum value.

2.5. Chl-a and TSS Algorithms

To generate Chl-a and TSS maps from the UAV and satellite imagery, the Rrs data were processed by different water-quality algorithms (OC-2 [31] and OC-3 [32] for Chl-a and [33] for TSS). Subsequently, water-quality maps were obtained in the vicinity of the Maltese coastline.

The OC-2 algorithm (presented in Equation (10)) was originally developed for SeaWiFS data and was later fine-tuned for the SeaBAM data. The OC-3 algorithm (Equation (11)) was developed to retrieve low and high Chl-a values and was applied to estuarine waters [31,51]. In this case study, we used the ratio (R) between blue (475 nm) and green (560 nm), as shown in Equations (10) and (11).

$$Chla \left(\frac{\text{mg}}{\text{m}^3} \right) = 10^{(0.341 - 3.0010 * R + 2.811 * R^2 - 2.041 * R^3)} + 0.040 \quad (10)$$

$$Chla \left(\frac{\text{mg}}{\text{m}^3} \right) = 10^{(0.283 - 2.753 * R + 1.457 * R^2 - 0.659 * R^3 - 1.403 * R^4)} \quad (11)$$

The multi-conditional algorithm tested by [16], which is based on the [33] model, considers the red (668 nm) band to be the most important for making these estimates. This was used to estimate the TSS concentrations and is based on Equation (12).

$$TSS \left(\frac{\text{mg}}{\text{L}} \right) = \frac{961 * Rrs_{(\lambda 668)}}{1 - Rrs_{(\lambda 668)} / 0.1728} + 29 \quad (12)$$

3. Results

3.1. Comparison of the R_{rs} Retrieval Methods from Individual UAV Captures

In this study, the multispectral UAV captures have been individually treated to extract the reflectance values of each pixel using the DPA and the DEG methods, as is described in Section 2.4.2. Obtaining in situ measurements without a boat is very difficult as the site is located under a cliff. Therefore, validations were performed with respect to the SfM orthomosaic that was considered to be the best approximation to reality. Figure 3 includes the linear regression models between the reflectance data obtained with the UAV individual captures and the orthomosaic generated by SfM photogrammetry. For this, 100 pixels were randomly selected to minimise computation time and memory requirements. In general, very positive results were obtained when applying both methods and the coefficient of determination (R^2) varied between 0.83 and 0.91, although an irregular value was found with the DPA method in the Cumnija dataset ($R^2 = 0.42$). The best correlations were obtained with the DEG method (specifically after its application over water areas) when it was compared to the DPA method.

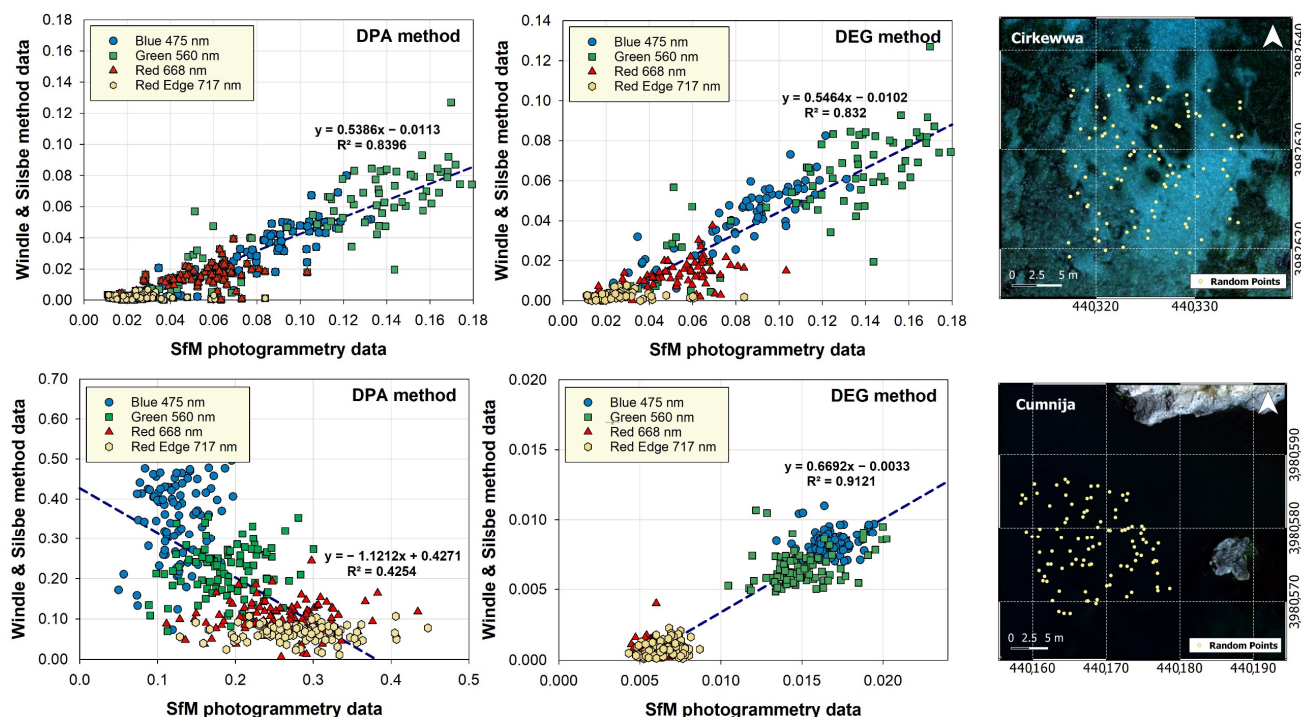


Figure 3. Pixel-by-pixel and band-by-band comparison between R_{rs} data (dimensionless) obtained by the DPA and the DEG methods, respectively, and the UAV photogrammetry. One hundred pixels ($n = 100$) were randomly selected and are also displayed in the figure.

The RMSE, MAE, and bias statistics were also calculated to assess the consistency between reflectance data (Table 1). As with R^2 , the DEG method was proven to provide statistical results closer to the photogrammetric reflectance data, although these values are close to 0 in all cases and are very similar between them. Irregular values were only found when applying the DPA to the Cumnija dataset and can probably be associated with the high sun glint during the UAV survey, the effects of the shadows, and the shallow water near the cliff, so that the reflectance values were affected by the influence of the rocky sea floor. In general terms, the reflectance values calculated by photogrammetry were higher than those retrieved manually (especially in the red-668 nm and red edge-717 nm bands), so that positive bias values with DPA and DEG methods indicated that the photogrammetric data overestimated the reflectance values when compared to the manually obtained UAV reflectance data.

Table 1. Statistics calculated (R^2 , RMSE, MAE and bias) for the linear regression models applied to the relationships between the UAV-retrieved reflectance data and the UAV photogrammetric reflectance data, comparing DPA and DEG methods.

		R^2	RMSE	MAE	Bias
Cirkewwa	DPA	0.84	0.050	0.044	0.044
	DEG	0.83	0.048	0.042	0.042
Čumnija	DPA	0.43	0.197	0.169	0.026
	DEG	0.91	0.007	0.007	0.006

3.2. Novel UAV Water-Mosaicking Method: Python Workflow

Once Rrs data was retrieved from the raw, multispectral UAV imagery, all the individual captures were grouped into an orthomosaic based on the information provided by the MicaSense metadata during the surveys. This was achieved with the CameraTransform Python package [48]. Apart from the yaw, pitch, and roll, the UAV latitude and longitude information were extracted. In addition, the averaged reflectance values for overlapping pixels were computed. However, although the water area covered was much higher by using this new technique, the aforementioned sun-glint effects over reflectance results (represented with white colours), and the absence of stitching between the captures, are still present in the generated orthomosaics. Figures 4 and 5 show the aquatic regions of the Cirkewwa and Čumnija study areas, respectively, manually mosaicked for each of the multispectral bands (with the exception of the NIR which, as was previously mentioned, is assumed to be equal to 0 in the retrieval methods).

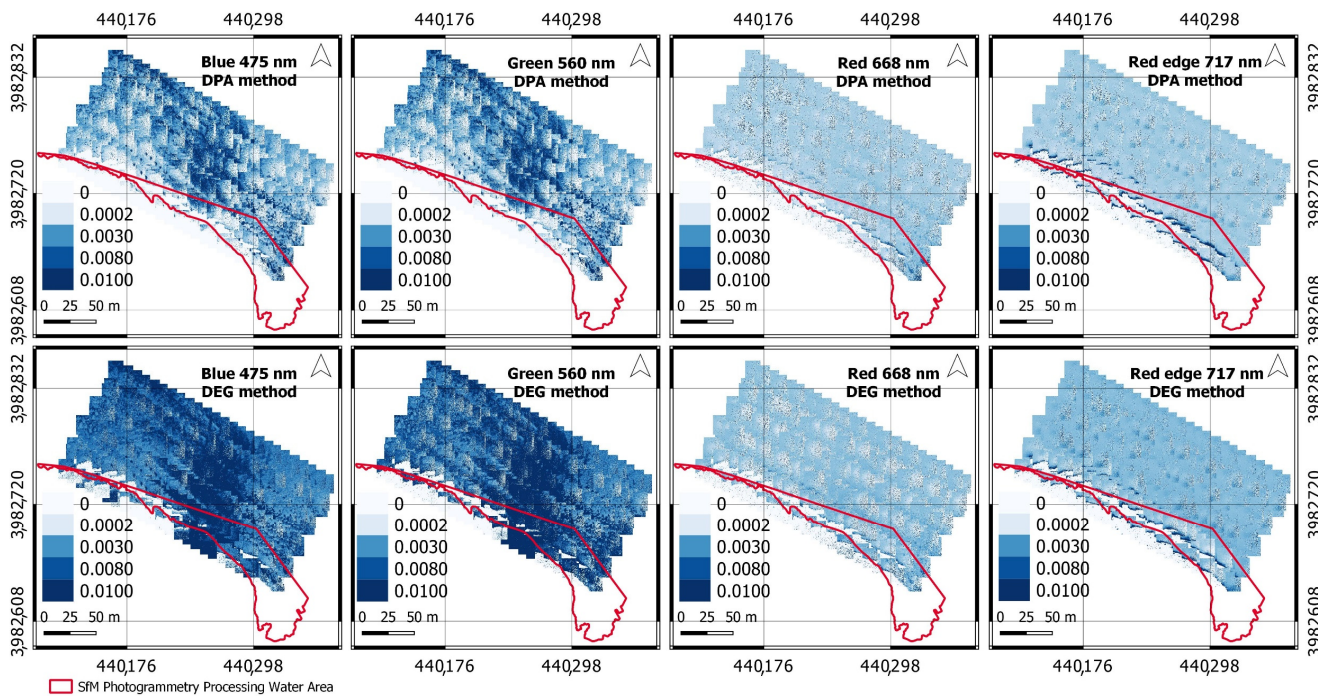


Figure 4. All-bands orthomosaics at Cirkewwa study location by using both the DPA and DEG methods for Rrs retrieval. Rrs values are given in sr^{-1} . The water area covered after SfM photogrammetric processing is marked in red.

3.3. Spectral Shape Comparison: UAV and Sentinel-2 Imagery

There are several factors that can affect the spectral response of sea water, such as turbidity, chlorophyll content, water depth, or the kind of substrate below the water [52,53]. However, and despite the aforementioned factors, blue and green bands generally show relatively high reflectance when compared with other bands [54]. In principle, for clear

waters as Maltese coastal waters, the highest reflectance is shown in the green region of the spectra, progressively decreasing until it reaches zero values in the near-infrared region [55]. Figure 6 represents the spectral shape after applying standardization to the reflectance values obtained with the DPA method, the DEG method, SfM photogrammetry, and S2 imagery at two different points in each study location.

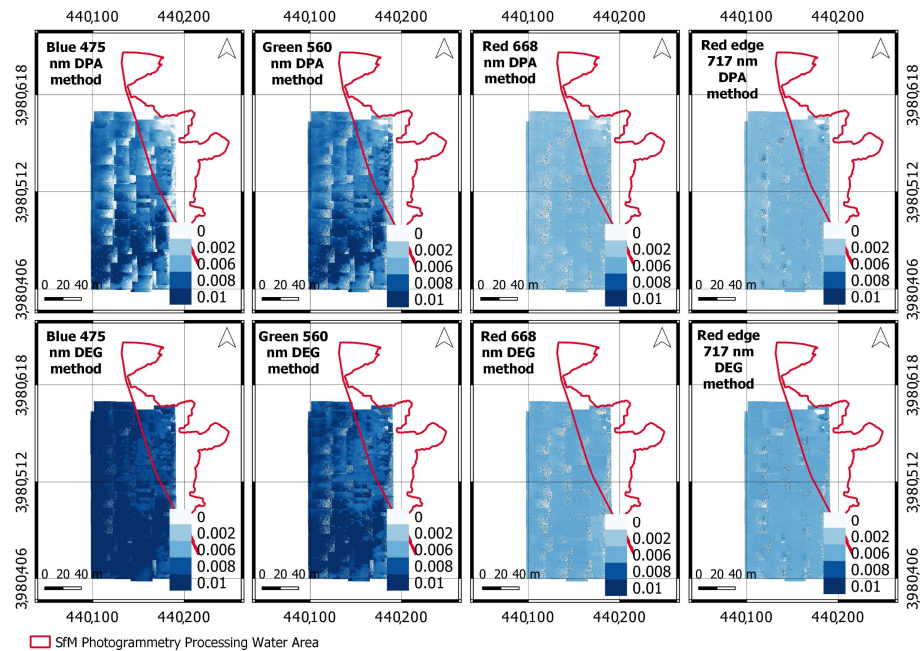


Figure 5. All-bands orthomosaics at Ćumnija study location by using both the DPA and DEG methods for Rrs retrieval. Rrs values are given in sr^{-1} . The water area covered after SfM photogrammetric processing is marked in red.

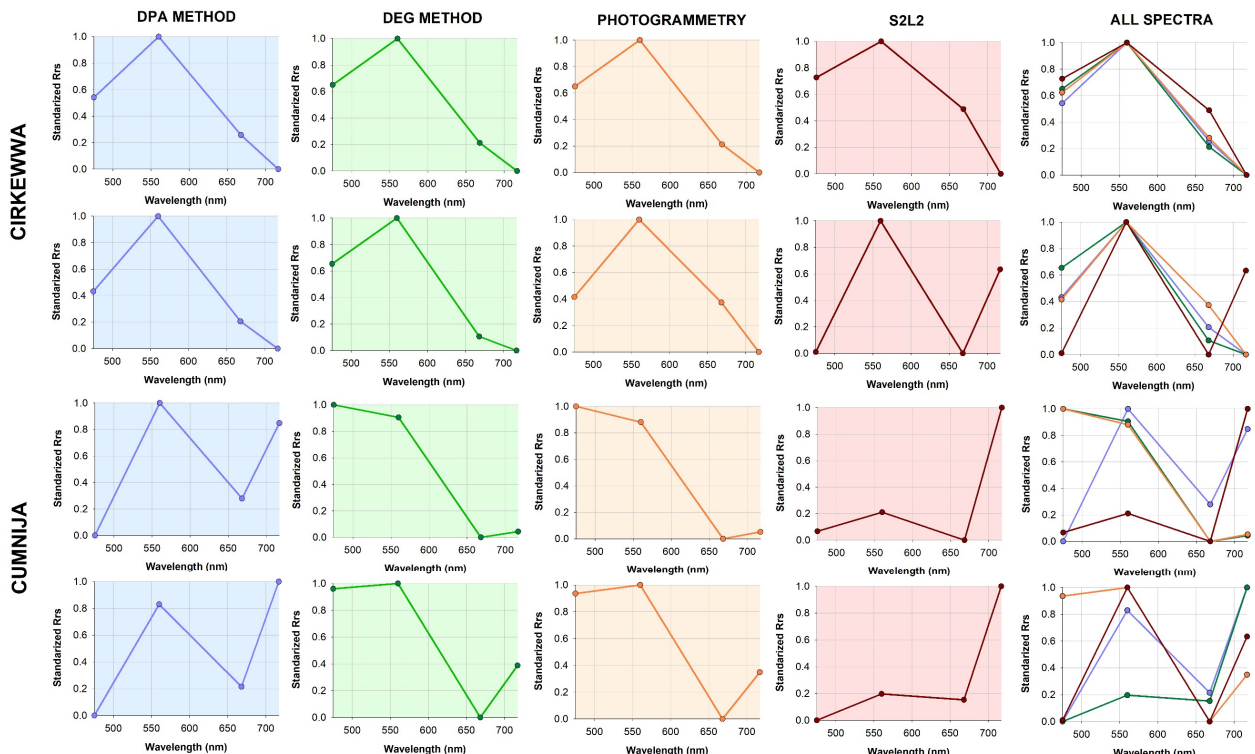


Figure 6. Water-reflectance spectra retrieved from the DPA method, the DEG method, SfM photogrammetry, and S2 imagery at two different points in each study location.

3.4. Water-Quality Algorithms (*Chl-a* and TSS) at Maltese Coastal Waters

The algorithms used to map the spatial distribution of the *Chl-a* and TSS concentrations at the Maltese coastal waters were applied, according to the optimal regression models listed in Table 1 and the similarity between different spectral shapes (Figure 6). Figure 7 shows the spatial distributions of *Chl-a* after applying the OC-2 [31] and OC-3 [32] algorithms to UAV and S2 data. Yellow pixels close to the coastline are mostly related to sun glint during the UAV surveys. However, these higher values at both study locations can also be attributed to the presence of *P. oceanica* meadows under the Maltese coastal waters as well as the shallow water depth near the coastline that makes the sediment at the bottom influence the reflection of light, resulting in higher *Chl-a* values. Although the sampling sites were chosen due to the probable discharges from the water treatment plants, this did not seem to be the case.

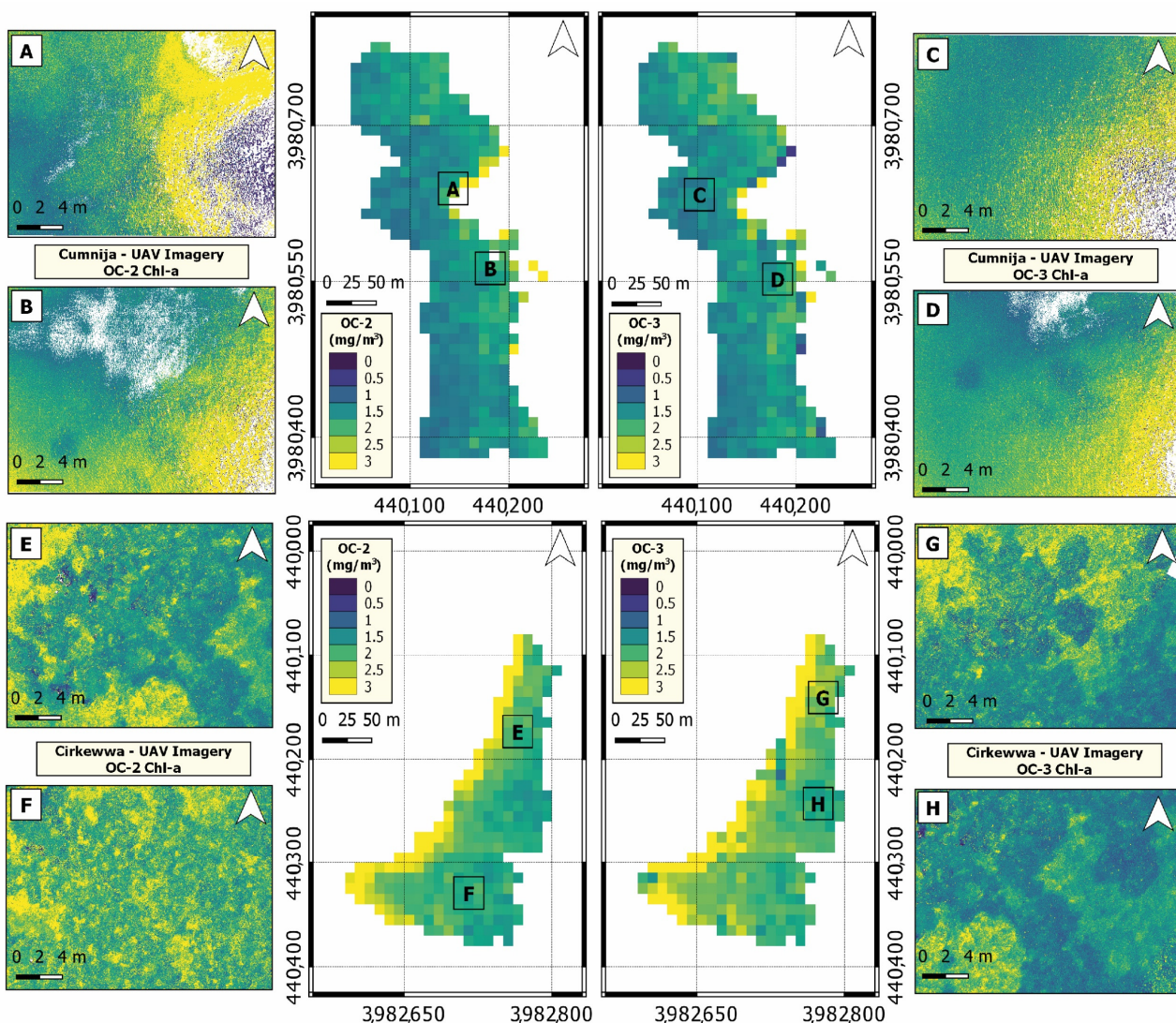


Figure 7. Spatial distribution of *Chl-a* for Čumnija and Cirkewwa using OC-2 [31] and OC-3 [32] algorithms. S2L2 *Chl-a* maps are represented in the middle of the figure, and subplots (A–H) refer to zoomed *Chl-a* UAV data at each study location.

Figure 8 shows the TSS maps generated after applying the algorithm presented in [16] based on the [33] model, using the red-668 nm band to UAV and S2 data. The results show how the use of the red band in clear waters (Cirkewwa) is clearly affected by the influence of sun glint and the reflection of light by the sediment in the shallower areas near

the coastline, which had a great influence on the results of the study. For this reason, the application of the TSS algorithm on UAV imagery offered an overestimation of S2 data.

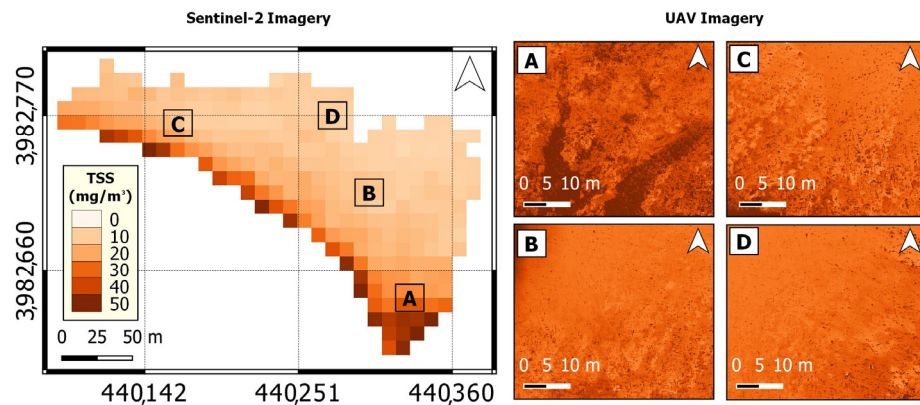


Figure 8. Spatial distribution of TSS for Cirkewwa using the [33] algorithm. The S2L2-TSS map is on the left, and subplots (A–D), referring to zoomed TSS UAV data, are on the right.

4. Discussion

4.1. Performance of the Reflectance-Retrieval Methods from Individual UAV Captures

The MicaSense RedEdge-MX multispectral camera fitted on the M600 Pro recorded individual DN captures for each band. The images were radiometrically corrected in order to be used as inputs within the water-quality parameters' retrieval algorithms. The DPA is one of the most reproducible methods for reflectance retrieval in clear waters, removing L_{SR} from visible wavelengths and thus reducing the influence of atmospheric effects and sun glint at the NIR wavelength. In contrast, the DEG method calculates a constant NIR brightness level that was deleted in each pixel for each wavelength.

The results obtained were compared pixel-by-pixel and band-by-band with the reflectance data obtained using a photogrammetric software. It was considered the most reliable data in the absence of in situ data, and previous research validated the accuracy of photogrammetry-derived products [5,29,56,57]. In particular, this study was limited by the distance from the coastline, since photogrammetric software works well when finding common points near coastal regions.

The computed statistics displayed in Figure 3 and Table 1 show a good fit between the different methods used. According to the R^2 values obtained, the DEG technique provided the best approximation of the photogrammetric data, as in [27]. In addition, both methods were found to have good RMSE, MAE, and bias errors, although the DPA method showed an abnormal R^2 value and worse statistics values for the Ćumnija site. Ref. [27] suggested that the DEG method is more recommendable to extract Rrs , except in open ocean waters without a strong influence of optically active properties. At Ćumnija, the shallowness of the water, the presence of rocks in the vicinity of the cliff, and the effect of the sun glint or the shadows on the seawater caused the DPA method to not work correctly. However, in Cirkewwa, a less-confined region with less influence from these factors, both methods worked well. This study shows that the method suggested by [27] to extract Rrs from raw, UAV individual captures works correctly, although it would be interesting to consider the variation of L_{sky} throughout the flight, since only the captures taken at a 40° angle at the beginning of the UAV survey were considered.

4.2. Performance and Considerations of the Mosaicking Method

One of the biggest challenges faced by UAV remote sensing is to elaborate and merge captures into a georeferenced orthomosaic having a centimetre-scale spatial resolution. Orthomosaics of small water bodies can be generated if the UAV captures contain enough common terrestrial features around the water body to enable the stitching of images. High-altitude flights could also be performed to cover larger areas. The reflectance values can be

extracted, for example, through the method described in this study. However, current UAV legislation imposed across Europe limits the maximum flight altitude to 120 m. Ref. [58] proposed alternative methods based on the use of statistical interpolation models, although values obtained through this method are considerably discordant with real ones.

In this study, a new method to mosaic individual UAV captures originating from the MicaSense multispectral sensor metadata and from the CameraTransform Python package was implemented to obtain reflectance maps for each multispectral band (Figures 4 and 5). Firstly, the obtained orthomosaics clearly showed a much higher water coverage when comparison to the SfM photogrammetric orthomosaics. In addition, the maps obtained generally showed a good georeferencing, although the information provided by the MicaSense sensor metadata was not entirely accurate and did not correctly consider the orientation of the UAV. This could be corrected by manually introducing the “heading_deg” parameter in the code, which forces the UAV capture to orient itself depending on the orientation of the sensor during the UAV survey. Secondly, the captures appeared overlapped between them (according to the frontal and side overlap established when programming the UAV flight plan), so that the results obtained are not considered reliable enough yet to replace SfM photogrammetry in mixed areas (including land and water), appearing as a misalignment such as the one observed on the coastline of the Ćumnija and Cirkewwa surveys. However, this code can be perfectly performed for ocean colour studies, as is demonstrated in this research, despite the strong influence of the sun glint and the proximity to the coastline. Finally, future work should focus on the elimination or minimisation of overlap between the UAV captures during the flights so that a cleaner final output can be generated.

4.3. Spectral Shape Analysis

The UAV and satellite sensor reflectance spectra for two water points at each study location are shown in Figure 6. In general, the DEG and photogrammetric methods show the previously described trend in the selected points at each location, with reflectance peaks at green and blue bands. However, abnormal values were observed in the spectral shapes (i) when applying the DPA method at Ćumnija, probably due to the high sun glint, the effects of the cliff shadows, and the influence of the rocky sea floor; and (ii) with S2 imagery, since the lower spatial resolution (10 m/pixel) includes more interpixel variability associated with the heterogeneity of the coastal areas and the proximity of both study locations to land. It is for this reason that, in the spectral curves of S2, a substantial increase in the RedEdge reflectance values was found when a progressive decrease to zero in the NIR was expected due to the absorption of infrared radiation by the water.

4.4. Water Quality at Maltese Coastal Waters

The *Chl-a* maps shown in Figure 7 indicate water-chlorophyll values that range between 0 to 3 mg/m³ for UAV and S2 data, respectively. As previously mentioned, such *Chl-a* values are higher than expected near the coastline, probably due to the influence of sun glint and a greater reflectance by the shallower sediment. If the order of magnitude of the results obtained in this study is compared with that of comparable research carried out to date with satellite data, it emerges that the two sets of values are quite similar. For example, ref. [51] tested the suitability of OC-2 and OC-3 algorithms with Sentinel-2 and Landsat 8 imagery in estimating *Chl-a* in the turbid coastal waters of the Bay of Bengal, obtaining pre-monsoon averaged values ranging between 1 and 4 mg/m³, post-monsoon averaged values ranging between 3 and 5 mg/m³, and during-winter-monsoon averaged values ranging between 4 and 6 mg/m³ with the OC-2 algorithm. Ref. [59] also used OC-2 and OC-3 algorithms with Landsat-8 data to extract surface *Chl-a* concentration in the Bushehr area of the Persian Gulf, obtaining averaged values between 0 and 4 mg/m³.

The TSS maps presented in Figure 8 also show overestimated values (between 30–40 mg/m³) with respect to the S2 data (between 10 and 20 mg/m³). This can also be attributed to the influence of sun glint and to the greater reflectance of the sea bottom in shallow waters. As with the *Chl-a* algorithms, the results are in the same order of magnitude as those obtained

in other research that focuses on the TSS estimation. Ref. [60] applied the algorithm to Formosat-5 images to estimate the total suspended matter (TSM) concentrations in a coastal region of Ha Long Bay (Vietnam), obtaining averaged TSS values ranging between 25 and 75 mg/m³. Ref. [33] also used the TSS algorithm on MODIS images to estimate the TSM for the coastal region of Ha Long Bay and obtained values in the range of 10 to 70 mg/m³.

The first attempt to apply remote-sensing techniques for water-quality monitoring purposes within Maltese waters was undertaken by [61], which involved a single-day comparison of Landsat-5 ocean colour, sea surface temperature, and water transparency data with in situ data. Since then, very few relevant studies which can serve as a reference for comparative purposes were conducted. Ref. [62] extracted moderate-spatial-resolution MODIS water-quality data close to the shoreline over a year and concluded that the lowest *Chl-a* values with the MedOC-4 algorithm [63] were obtained between April and May and varied between 0.04 and 1.37 mg/m³. In addition, by applying the OC-4 and AD4 algorithms on MODIS data, ref. [64] estimated a *Chl-a* annual average of 0.216 mg/m³. More recently, the WaterColours Project explored the use of a long, ocean-colour Sentinel-3 OLCI imagery dataset for the estimation of *Chl-a* concentration in the coast and shelf areas of the Maltese Islands, providing data continuity for ENVISAT's MERIS imagery between 2002 and 2012. Ref. [65] provided the highest resolution *Chl-a* data until today (300 m spatial resolution) in a study area near the south coast of Malta. Average values of *Chl-a* between 0 and 1 mg/m³ for the month of May were obtained.

This study represents the most accurate approximation of water quality near the coastline in Malta using high-resolution satellite data (10 m spatial resolution) and its first estimation through the use of centimetre-scale UAV data. The water-quality parameters computed from UAV data have a much higher spatial resolution than the 300 m provided by the OLCI data. In addition, the *Chl-a* values are quite similar to those previously obtained in the vicinity of the Maltese coastline, ranging between 0 and 1.5 mg/m³. However, there is no background about TSS values at the Maltese coastline, this study being considered the first TSS approximation with values ranging between 10–20 mg/m³.

5. Conclusions

Different methodologies suggest that water-quality monitoring techniques hinging on remote-sensing protocols can be improved through the fusion of satellite and UAV data. Through the current study, the applicability of SfM photogrammetry and its compatibility with the high-resolution S2 satellite data in near-shore regions was demonstrated. The limitations imposed by the sun-glint effect and the reflection of light by shallow-water sediment, were also considered. The results obtained with the different methods applied in the current study proved to be very similar to those achieved through the sole use of photogrammetric data. Although preliminary results indicate that the mosaicking technique based on the multispectral camera metadata is acceptable, future research can focus on improving the developed framework to extract more accurate geolocation of individual UAV captures and to reduce the overlapping effects between the images during the flights.

Supplementary Materials: The following supporting information can be downloaded at: <https://github.com/alrova96/UAV-Water-Mosaicking-Code> (accessed on 27 November 2022).

Author Contributions: A.R. contributed writing the first draft, as well designing figures and geoprocessing data; A.R., A.G. and E.C. carried out the UAV surveys, collecting optical and multispectral data; I.C. and A.G. prepared all Sentinel-2 data and processed atmospheric corrections for satellite imagery; All authors have contributed in the writing—review, editing and supervision of the published version of the manuscript. All authors have read and agreed to the published version of the manuscript.

Funding: This research was funded by grants PY20-00244 SAT4ALGAE Junta de Andalucía, RTI2018-098784-J-I00 (Sen2Coast Project), IJC2019-039382-I (Juan de la Cierva-Incorporación), funded by MCIN/AEI/1 0.13039/501100011033, and supported by “ERDF A way of making Europe”. A.R. is supported by grant FPU19/04557, funded by the Ministry of Universities of the Spanish Government, and the ERASMUS+ KA/103 grant funded by the University of Cádiz. This work represents a contribution to the CSIC Thematic Interdisciplinary Platform PTI TELEDETECT.

Data Availability Statement: Not applicable.

Acknowledgments: The authors would like to thank the European Space Agency, the European Commission, and the Copernicus programme for distributing Sentinel-2 imagery. We also thank Sergio Heredia Carmona from ICMAN-CSIC for his contribution in the elaboration of the python code.

Conflicts of Interest: The authors declare no conflict of interest.

References

1. Gai, Y.; Yu, D.; Zhou, Y.; Yang, L.; Chen, C.; Chen, J. An Improved Model for Chlorophyll-a Concentration Retrieval in Coastal Waters Based on UAV-Borne Hyperspectral Imagery: A Case Study in Qingdao, China. *Water* **2022**, *12*, 2769. [[CrossRef](#)]
2. Moses, W.J.; Gitelson, A.A.; Perk, R.L.; Gurlin, D.; Rundquist, D.C.; Leavitt, B.C.; Barrow, T.M.; Brakhage, P. Estimation of chlorophyll-a concentration in turbid productive waters using airborne hyperspectral data. *Water Res.* **2012**, *46*, 993–1004. [[CrossRef](#)] [[PubMed](#)]
3. Baek, J.; Jo, Y.; Kim, W.; Lee, J.; Jung, D.; Kim, D.; Nam, J. A New Algorithm to Estimate Chlorophyll-A Concentrations in Turbid Yellow Sea Water Using a Multispectral Sensor in a Low-Altitude Remote Sensing System. *Remote Sens.* **2019**, *11*, 2257. [[CrossRef](#)]
4. Lu, Q.; Si, W.; Wei, L.; Li, Z.; Xia, Z.; Ye, S.; Xia, Y. Retrieval of Water Quality from UAV-Borne Hyperspectral Imagery: A Comparative Study of Machine Learning Algorithms. *Remote Sens.* **2021**, *13*, 3928. [[CrossRef](#)]
5. Guimarães, T.T.; Veronez, M.R.; Koste, E.C.; Gonzaga, L.; Bordin, F.; Inocencio, L.C.; Larocca, A.P.C.; De Oliveira, M.Z.; Vitti, D.C.; Mauad, F.F. An Alternative Method of Spatial Autocorrelation for Chlorophyll Detection in Water Bodies Using Remote Sensing. *Sustainability* **2017**, *9*, 416. [[CrossRef](#)]
6. Doney, S.C.; Ruckelshaus, M.; Duffy, J.E.; Barry, J.P.; Chan, F.; English, C.A.; Galindo, H.M.; Grebmeier, J.M.; Hollowed, A.B.; Knowlton, N.N.; et al. Climate Change Impacts on Marine Ecosystems. *Ann. Rev. Mar. Sci.* **2012**, *4*, 11–17. [[CrossRef](#)]
7. Gray, P.; Larsen, G.; Johnston, D.W. Drones address an observational blind spot for biological oceanography. *Front. Ecol. Environ.* **2022**, *1*, 413–421. [[CrossRef](#)]
8. Wang, J.; Zhang, Y.; Yang, F.; Cao, X.; Bai, Z.; Zhu, J.; Chen, E.; Li, Y.; Ran, Y. Spatial and temporal variations of chlorophyll-a concentration from 2009 to 2012 in Poyang Lake, China. *Environ. Earth Sci.* **2015**, *73*, 4063–4075. [[CrossRef](#)]
9. Birtwell, I.K.; Farrell, M.; Jonsson, A. *The Validity of Including Turbidity Criteria for Aquatic Resource Protection in Land Development Guideline (Pacific and Yukon Region)*; Canadian Manuscript Report of Fisheries and Aquatic Sciences; Fisheries and Oceans Canada: Vancouver, BC, Canada, 2008; Volume 2852, ISSN 0706-6473.
10. Xu, J.; Gao, C.; Wang, Y. Extraction of Spatial and Temporal Patterns of Concentrations of Chlorophyll-a and Total Suspended Matter in Poyang Lake Using GF-1 Satellite Data. *Remote Sens.* **2020**, *12*, 622. [[CrossRef](#)]
11. Ying, H.; Xia, K.; Huang, X.; Feng, H.; Yang, Y.; Du, X.; Huang, L. Evaluation of water quality based on UAV images and the IMP-MPP algorithm. *Ecol. Inform.* **2021**, *61*, 101239. [[CrossRef](#)]
12. Blondeau-Patissier, D.; Gower, J.F.R.; Dekker, A.G.; Phinn, S.R.; Brando, V.E. A review of ocean color remote sensing methods and statistical techniques for the detection, mapping and analysis of phytoplankton blooms in coastal and open oceans. *Prog. Oceanogr.* **2014**, *123*, 123–144. [[CrossRef](#)]
13. Cheng, K.H.; Chan, S.N.; Lee, J.H.W. Remote sensing of coastal algal blooms using unmanned aerial vehicles. *Mar. Pollut. Bull.* **2020**, *152*, 110889. [[CrossRef](#)] [[PubMed](#)]
14. Cillero-Castro, C.; Domínguez-Gómez, J.A.; Delgado-Marín, J.; Hinojo, B.A.; Cereijo, J.L.; Cheda, F.A.; Díaz-Varela, R. An UAV and Satellite Multispectral Data Approach to Monitor Water Quality in Small Reservoirs. *Remote Sens.* **2020**, *12*, 1514. [[CrossRef](#)]
15. Mobley, C.D. Estimation of the remote-sensing reflectance from above-surface measurements. *Appl. Opt.* **1999**, *38*, 7442–7455. [[CrossRef](#)] [[PubMed](#)]
16. Caballero, I.; Steinmetz, F.; Navarro, G. Evaluation of the First Year of Operational Sentinel-2A Data for Retrieval of Suspended Solids in Medium- to High- Turbidity Waters. *Remote Sens.* **2018**, *10*, 982. [[CrossRef](#)]
17. Gitelson, A.A.; Dall’Olmo, G.; Moses, W.; Rundquist, D.C.; Barrow, T.; Fisher, T.R.; Gurlin, D.; Holz, J. A simple semi-analytical model for remote estimation of chlorophyll-a in turbid waters: Validation. *Remote Sens. Environ.* **2008**, *112*, 3582–3593. [[CrossRef](#)]
18. Gilerson, A.A.; Gitelson, A.A.; Zhou, J.; Gurlin, D.; Moses, W.; Ioannou, I.; Ahmed, S.A. Algorithms for remote estimation of chlorophyll-a in coastal and inland waters using red and near infrared bands. *Opt. Express* **2010**, *18*, 24109–24125. [[CrossRef](#)]
19. Hu, C.M.; Carder, K.L.; Muller-Karger, F.E. Atmospheric correction of SeaWiFS imagery over turbid coastal waters: A practical method. *Remote Sens. Environ.* **2000**, *74*, 195–206. [[CrossRef](#)]
20. Huang, W.; Chen, S.; Yang, X.; Johnson, E. Assessment of Chlorophyll-a Variations in High- and Low- Flow Seasons in Apalachicola Bay by MODIS 250-m remote sensing. *Environ. Monit. Assess.* **2014**, *186*, 8329–8342. [[CrossRef](#)]

21. Nazeer, M.; Nichol, J.E. Development and application of a remote sensing-based Chlorophyll-a concentration prediction model for complex coastal Waters of Hong Kong. *J. Hydrol.* **2016**, *532*, 80–89. [CrossRef]
22. Rodríguez-Benito, C.V.; Navarro, G.; Caballero, I. Using Copernicus Sentinel-2 and Sentinel-3 data to monitor harmful algal blooms in Southern Chile during the COVID-19 lockdown. *Mar. Pollut. Bull.* **2020**, *161(A)*, 111722. [CrossRef] [PubMed]
23. Syariz, M.A.; Lin, C.H.; Nguyen, M.V.; Jaelani, L.M.; Blanco, A.C. WaterNet: A Convolutional Neural Network for Chlorophyll-a Concentration Retrieval. *Remote Sens.* **2020**, *12*, 47–57. [CrossRef]
24. Yang, W.; Matsushita, B.; Chen, J.; Fukushima, T.; Ma, R. An enhanced three-band index for estimating chlorophyll-a in turbid Case-II waters: Case studies of lake Kasumigaura, Japan, and Lake Dianchi, China. *IEEE Geosci. Remote. Sens. Lett.* **2010**, *7*, 655–659. [CrossRef]
25. Choo, Y.; Kang, G.; Kim, D.; Lee, S. A study on the evaluation of water-bloom using image processing. *Environ. Sci. Pollut. Res.* **2018**, *25*, 36775–36780. [CrossRef]
26. Gray, P.; Windle, A.E.; Dale, J.; Savelyev, I.B.; Johnson, Z.I.; Silsbe, G.M.; Larsen, G.D.; Johnston, D.W. Robust ocean color from drones: Viewing geometry, sky reflection removal, uncertainty analysis, and a survey of the Gulf Stream front. *Limnol. Oceanogr. Methods* **2022**, *20*, 656–673. [CrossRef]
27. Windle, A.E.; Silsbe, G.M. Evaluation of Unoccupied Aircraft System (UAS) Remote Sensing Reflectance Retrievals for Water Quality Monitoring in Coastal Water. *Front. Environ. Sci.* **2021**, *9*, 674247. [CrossRef]
28. Johansen, K.; Dunne, A.F.; Tu, Y.; Almarsharawi, S.; Jones, B.H.; McCabe, M.F. Dye tracing and concentration mapping in coastal Waters using unmanned aerial vehicles. *Sci. Rep.* **2022**, *12*, 1141. [CrossRef]
29. Arango, J.G.; Nairn, R.W. Prediction of Optical and Non-Optical Water Quality Parameters in Oligotrophic and Eutrophic Aquatic Systems Using a Small Unmanned Aerial System. *Drones* **2020**, *4*, 1. [CrossRef]
30. Olivetti, D.; Roig, H.; Martinez, J.; Borges, H.; Ferreira, A.; Casari, R.; Salles, L.; Malta, E. Low-Cost Unmanned Aerial Multispectral Imagery for Siltation Monitoring in Reservoirs. *Remote Sens.* **2020**, *12*, 1855. [CrossRef]
31. O'Reilly, J.E.; Maritorena, S.; Mitchell, B.G.; Siegal, D.A.; Carder, K.L.; Graver, S.A.; Kahru, M.; McClain, C. Ocean color chlorophyll algorithms for SeaWiFS. *J. Geophys. Res.* **1998**, *103*, 24937–24953. [CrossRef]
32. Morel, A.; Maritorena, S. Bio-optical properties of oceanic waters: A reappraisal. *J. Geophys. Res.* **2001**, *106*, 7163–7180. [CrossRef]
33. Nechad, B.; Ruddick, K.G.; Park, Y. Calibration and validation of a generic multisensor algorithm for mapping of total suspended matter in turbid waters. *Remote Sens. Environ.* **2010**, *114*, 854–866. [CrossRef]
34. Hartfield, L.; Soupir, M.; Kanwar, R.S. Malta's Water Scarcity Challenges: Past, Present, and Future Mitigation Strategies for Sustainable Water Supplies. *Sustainability* **2020**, *12*, 9835. [CrossRef]
35. Reitano, R. Water harvesting and water collection systems in Mediterranean area. The case of Malta. *Procedia Eng.* **2011**, *21*, 81–88. [CrossRef]
36. Bartolo, A.G.; Tsiamis, K.; Küpper, F.C. Identifying hotspots of non-indigenous species' high impact in the Maltese islands (Central Mediterranean Sea). *Mar. Poll. Bull.* **2021**, *164*, 112016. [CrossRef]
37. Borg, J.A.; Attrill, M.J.; Rowden, A.A.; Schembri, P.J.; Jones, M.B. Architectural characteristics of two bed types of the seagrass Posidonia oceánica over different spatial scales. *Estuar. Coast. Shelf Sci.* **2005**, *62*, 667–678. [CrossRef]
38. Borg, J.A.; Schembri, P.J. Preliminary data on bathymetric and temporal changes in the morphology of a Maltese Posidonia oceánica (L.) Delile meadow. *Int. Pour L'exploration Sci. Mer Méditerranée* **1995**, *34*, 20.
39. Sánchez-Lizaso, J.L.; Romero, J.; Ruiz, J.; Gacia, E.; Buceta, J.L.; Invers, O.; Fernández, Y.; Mas, J.; Ruíz-Mateo, A.; Manzanera, M. Salinity tolerance of the Mediterranean seagrass Posidonia oceánica: Recommendations to minimize the impact of brine discharges from desalination plants. *Desalination* **2008**, *221*, 602–607. [CrossRef]
40. European Space Agency. *Sentinel-2 User Handbook*; ESA Standard Document; European Space Agency: Paris, France, 2015. Available online: https://sentinel.esa.int/documents/247904/685211/Sentinel-2_User_Handbook_ed (accessed on 27 November 2022).
41. European Space Agency. *Sentinel-2 MSI Technical Guide*. 2017. Available online: <https://earth.esa.int/web/sentinel/technicalguides/sentinel-2-msi> (accessed on 27 November 2022).
42. Vanhellemont, Q.; Ruddick, K. Atmospheric correction of metre-scale optical satellite data for inland and coastal water applications. *Remote Sens. Environ.* **2018**, *216*, 586–597. [CrossRef]
43. Vanhellemont, Q. Adaptation of the dark spectrum fitting atmospheric correction for aquatic applications of the Landsat and Sentinel-2 archives. *Remote Sens. Environ.* **2019**, *225*, 175–192. [CrossRef]
44. Wei, J.; Lee, Z.; Shang, S. A system to measure the data quality of spectral remote-sensing reflectance of aquatic environments. *J. Geophys. Res.* **2016**, *121*, 8189–8207. [CrossRef]
45. MicaSense. Image Processing Tutorials. 2022. Available online: <https://github.com/micasense/imageprocessing/actions> (accessed on 27 November 2022).
46. Hochberg, E.J.; Andréfouet, S.; Tyler, M.R. Sea Surface Correction of High Spatial Resolution Ikonos Images to Improve Bottom Mapping in Near-Shore Environments. *IEEE Trans. Geosci. Remote Sens.* **2003**, *41*, 1724–1729. [CrossRef]
47. Hedley, J.D.; Harbone, A.R.; Mumby, P.J. Technical Note: Simple and Robust Removal of Sun Glint for Mapping Shallow-water Benthos. *Int. J. Remote Sens.* **2005**, *26*(10), 2107–2112. [CrossRef]
48. Gerum, R.; Richter, S.; Winterl, A.; Mark, M.; Fabry, B.; Le Bohec, C.; Zitterbart, D.P. CameraTransform: A Python package for perspective corrections and image mapping. *SoftwareX* **2019**, *10*, 100333. [CrossRef] [PubMed]

49. Seegers, B.N.; Stumpf, R.P.; Schaeffer, B.A.; Loftin, K.A.; Werdell, P.J. Performance metrics for the assessment of satellite data products: An ocean color case study. *Opt. Express* **2018**, *26*, 7404–7422. [[CrossRef](#)]
50. Douay, F.; Verpoorter, C.; Duong, G.; Spilmont, N.; Gevaert, F. New Hyperspectral Procedure to Discriminate Intertidal Macroalgae. *Remote Sens.* **2022**, *14*, 346. [[CrossRef](#)]
51. Poddar, S.; Chacko, N.; Swain, D. Estimation of Chlorophyll-a in Northern Coastal Bay of Bengal Using Landsat-8 OLI and Sentinel-2 MSI Sensors. *Front. Mar. Sci.* **2019**, *6*, 598. [[CrossRef](#)]
52. Gitelson, A. The peak near 700 nm on radiance spectra of algae and water: Relationships of its magnitude and position with chlorophyll concentration. *Int. J. Remote Sens.* **1992**, *17*, 3367–3373. [[CrossRef](#)]
53. Maritorena, S.; Morel, A.; Gentili, B. Diffuse reflectance of oceanic shallow waters: Influence of water Depth and bottom albedo. *Limnol. Oceanogr.* **1994**, *39*, 1689–1703. [[CrossRef](#)]
54. Ma, S.; Zhou, Y.; Gowda, P.H.; Dong, J.; Zhang, G.; Kakani, V.G.; Wagle, P.; Chen, L.; Flynn, K.C.; Jiang, W. Application of the water-related spectral reflectance indices: A review. *Ecol. Indic.* **2019**, *98*, 68–79. [[CrossRef](#)]
55. Malinowski, R.; Groom, G.; Schwanghart, W.; Heckrath, G. Detection and Delineation of Localized Flooding from WorldView-2 Multispectral Data. *Remote Sens.* **2015**, *7*, 14853–14875. [[CrossRef](#)]
56. Dias, R.L.S.; da Silva, D.D.; Fernandes-Filho, E.I.; do Amaral, C.H.; dos Santos, E.P.; Marques, J.F.; Veloso, G.V. Machine learning models applied to TSS estimation in a reservoir using multispectral sensor onboard to RPA. *Ecol. Inform.* **2021**, *65*, 101414. [[CrossRef](#)]
57. Román, A.; Navarro, G.; Caballero, I.; Tovar-Sánchez, A. High-spatial resolution UAV multispectral data complementing satellite imagery to characterize a chinstrap penguin colony ecosystem on Deception Island (Antarctica). *GIsci Remote Sens.* **2022**, *59*, 1159–1176. [[CrossRef](#)]
58. Arango, J.G.; Holzbauer-Schweitzer, B.K.; Nairn, R.W.; Knox, R.C. Generation of Geolocated and Radiometrically Corrected True Reflectance Surfaces in the Visible Portion of the Electromagnetic Spectrum over Large Bodies of Water Using Images from sUAS. *J. Unmanned Veh. Syst.* **2020**, *8*, 172–185. [[CrossRef](#)]
59. Tehrani, N.; Janalipour, M.; Babaei, H. Estimating Water Surface Chlorophyll-a Concentration by Big Remote Sensing Data in the Persian Gulf, Bushehr. *Remote Sens. Earth Syst. Sci.* **2021**, *4*, 87–95. [[CrossRef](#)]
60. Chau, P.; Wang, C. Estimation of Total Suspended Matter Concentration of Ha Long Bay, Vietnam, from Formosat-5 Image. *J. Mar. Sci. Eng.* **2022**, *10*, 441. [[CrossRef](#)]
61. Geraci, A.L.; Fargione, G.A.; Axiak, V.; Tabone Adami, E. Monitoring of environmental water quality of Maltese coastal waters using remote sensing techniques. *Remote Sens.* **1997**, *96*, 241.
62. Deidun, A.; Drago, A.; Gauci, A.; Galea, A.; Azzopardi, J.; Mélin, F. A first attempt at testing correlation between MODIS ocean colour data and in situ chlorophyll-a measurements within Maltese coastal waters. *Proc. SPIE* **2016**, *8175*, 176–183. [[CrossRef](#)]
63. Volpe, G.; Santoleri, R.; Vellucci, V.; Ribera d’Alcalà, M.; Marullo, S.; D’Ortenzio, F. The colour of the Mediterranean Sea: Global versus regional bio-optical algorithms evaluation and implication for satellite chlorophyll estimates. *Remote Sens. Environ.* **2007**, *107*, 625–638. [[CrossRef](#)]
64. Saliba, M. Phytoplankton Dynamics in Maltese Coastal Waters (Central Mediterranean) Using In Situ, Remote Sensing Methods, and Modelling Techniques. Master’s Thesis, Prifysgol Bangor University, School of Ocean Sciences (Anglesey), Menai Bridge, UK, 2017.
65. Gauci, A.; Misra, A.; Krlovic, N.; Drago, A.; Ciani, D.; Falcini, F. The WaterColours Project—Preliminary Assessment of Chlorophyll-a Variability in the Malta Shelf Area. In Proceedings of the IEEE International Geoscience and Remote Sensing Symposium, Brussels, Belgium, 11–16 July 2021. [[CrossRef](#)]

Disclaimer/Publisher’s Note: The statements, opinions and data contained in all publications are solely those of the individual author(s) and contributor(s) and not of MDPI and/or the editor(s). MDPI and/or the editor(s) disclaim responsibility for any injury to people or property resulting from any ideas, methods, instructions or products referred to in the content.